# Continuous dynamical decoupling of a single diamond nitrogen-vacancy center spin with a mechanical resonator

E. R. MacQuarrie, T. A. Gosavi, S. A. Bhave, and G. D. Fuchs

Phys. Rev. B **92**, 224419 — Published 14 December 2015

DOI: 10.1103/PhysRevB.92.224419

# Continuous dynamical decoupling of a single diamond nitrogen-vacancy center spin with a mechanical resonator

E. R. MacQuarrie,[1] T. A. Gosavi,[1] S. A. Bhave,[2] and G. D. Fuchs[1,*]

[1] *Cornell University, Ithaca, NY 14853*
[2] *Purdue University, West Lafayette, IN 47907*

Inhomogeneous dephasing from uncontrolled environmental noise can limit the coherence of a quantum sensor or qubit. For solid state spin qubits such as the nitrogen-vacancy (NV) center in diamond, a dominant source of environmental noise is magnetic field fluctuations due to nearby paramagnetic impurities and instabilities in a magnetic bias field. In this work, we use ac stress generated by a diamond mechanical resonator to engineer a dressed spin basis in which a single NV center qubit is less sensitive to its magnetic environment. For a qubit in the thermally isolated subspace of this protected basis, we prolong the dephasing time $T_2^*$ from $2.7 \pm 0.1$ $\mu$s to $15 \pm 1$ $\mu$s by dressing with a $\Omega/2\pi = 581 \pm 2$ kHz mechanical Rabi field. Furthermore, we develop a model that quantitatively predicts the relationship between $\Omega$ and $T_2^*$ in the dressed basis. Our model suggests that a combination of magnetic field fluctuations and hyperfine coupling to nearby nuclear spins limits the protected coherence time over the range of $\Omega$ accessed here. We show that amplitude noise in $\Omega$ will dominate the dephasing for larger driving fields.

PACS numbers: 76.30.Mi, 63.20.kp, 76.60.Jx

## I. INTRODUCTION

The triplet spin of the nitrogen-vacancy (NV) center in diamond has become a foundational component in both quantum metrology and future quantum information technologies[1,2]. For sensing, the inhomogeneous dephasing time $T_2^*$ of an NV center spin qubit can limit sensitivity to quasi-static fields. For quantum information applications, $T_2^*$ can limit the number and the duration of gate operations that a qubit can undergo. Pulsed dynamical decoupling (PDD) techniques based on the principle of spin echoes refocus inhomogeneous dephasing and can extend $T_2^*$ to the homogeneous spin dephasing time $T_2$ or longer[3–8]. These periodic pulse sequences enable precision sensing and long-lived quantum states, but they come with drawbacks. They usually limit sensing to a narrow bandwidth and erase signal built up from quasi-static fields. Moreover, commuting echo pulses with gate operations makes decoupling during multi-qubit gates a nontrivial task[9].

Continuous dynamical decoupling (CDD) offers an alternative method for prolonging $T_2^*$ that can be used when the limitations of PDD become too restrictive. NV center CDD protocols forego the standard Zeeman spin state basis $\{(m_s =) + 1, 0, -1\}$ in favor of an engineered basis in which the "dressed" eigenstates are less sensitive to environmental noise than the bare spin states[10–19]. For an NV center spin qubit, magnetic field fluctuations from nearby paramagnetic impurities and instabilities in a magnetic bias field typically dominate dephasing. A qubit composed of dressed states designed to be more robust to these fluctuations could have a prolonged $T_2^*$ and could be used for precision sensing of quasi-static, non-magnetic fields such as temperature[20] or strain. For quantum information processing, CDD allows decoupling to continue during gate operations, thus protecting both qubit and gate from dephasing[12,14].

NV center CDD has typically been performed by magnetically driving the $|0\rangle \leftrightarrow |+1\rangle$ and $|0\rangle \leftrightarrow |-1\rangle$ spin transitions. Advances in diamond mechanical resonator fabrication[21–26] have enabled the use of ac lattice strain to coherently drive the magnetically forbidden $|+1\rangle \leftrightarrow |-1\rangle$ spin transition as shown in Fig. 1a[27]. This has in turn enabled mechanical CDD[28] in which continuous driving of the $|+1\rangle \leftrightarrow |-1\rangle$ transition creates a dressed basis that cannot be accessed with conventional magnetic spin control. The mechanically dressed basis has eigenstates $\{0, m, p\}$ where $|m\rangle$ and $|p\rangle$ are mixtures of only $|+1\rangle$ and $|-1\rangle$. The $|+1\rangle$ and $|-1\rangle$ states respond diametrically to magnetic fields, making $|m\rangle$ and $|p\rangle$ less sensitive to magnetic field fluctuations than their undressed constituents.

In this work, we perform mechanical CDD to prolong $T_2^*$ of single NV centers and quantify how $T_2^*$ scales with the mechanical dressing field. We determine that, within a thermally isolated subspace of the mechanically dressed basis, a combination of magnetic field fluctuations and coupling to unpolarized nuclear spins limits mechanical CDD over the range of cw dressing fields accessible to our device. Using experiments and theory, we show that for larger driving fields amplitude noise in the mechanical dressing field will become the dominant source of dephasing.

Compared to magnetic CDD protocols, mechanically dressing the NV center spin has the key benefit that the $|0\rangle$ state is left unperturbed. This eliminates the need to adiabatically dress and undress the NV center before and after each measurement—a process that can take as long as 50 $\mu$s each way[14]. Moreover, the Rabi fields generated by a mechanical resonator are noise filtered above a cutoff frequency $\omega_c$ determined by the quality factor $Q$ and the frequency of the resonance mode $\omega_{\mathrm{mech}}$. This is a valuable feature since driving field noise has previously limited magnetic CDD efforts[13,14,16,29–31].

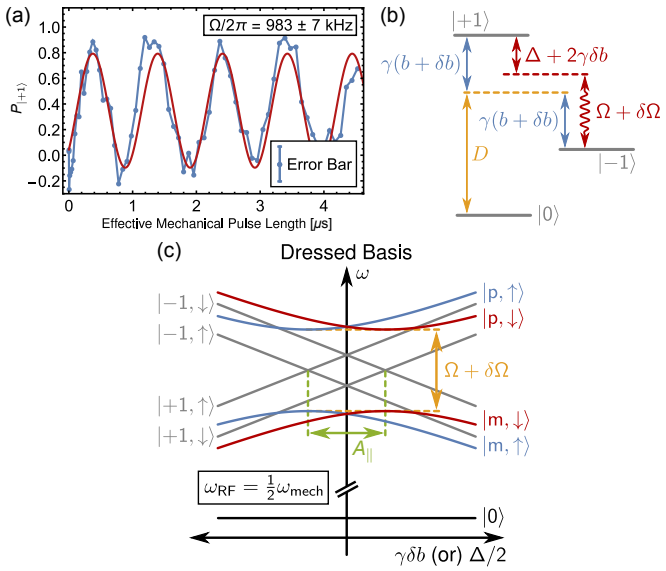


FIG. 1. (a) Mechanically driven Rabi oscillations between the $|-1\rangle$ and $|+1\rangle$ states of a single NV center within the $m_I = +1$ sublevel of the $^{14}$N hyperfine manifold (measurement details in Appendix A). (b) NV center Zeeman states subject to a static magnetic field $b + \delta b$ and a mechanical driving field $\Omega + \delta\Omega$. (c) Energies of the undressed and dressed eigenstates plotted as a function of both $\gamma\delta b$ and $\Delta/2$ in a reference frame rotating at $\omega_{RF} = \frac{1}{2}\omega_{\mathrm{mech}}$. We include hyperfine sublevels from a nearby $^{13}$C nuclear spin coupled with a strength $A_\parallel$.

## II. MECHANICALLY DRESSED STATES

Our derivation of the mechanically dressed energy levels begins in the conventional $\{+1, 0, -1\}$ Zeeman basis. As depicted in Fig. 1b, we consider a static magnetic field $b$ aligned along the NV center symmetry axis that is subject to fluctuations $\delta b$ and a mechanical driving field $\Omega$ that is subject to amplitude fluctuations $\delta\Omega$. We work within the $m_I = +1$ sublevel of the $^{14}$N hyperfine manifold. In diamonds with a natural distribution of carbon isotopes, nearby $^{13}C$ nuclear spins typically couple to the NV center spin. Weak coupling to a single $^{13}$C spin is described by the hyperfine perturbation $H_C = A_\parallel S_z I_z$ where $S_z$ and $I_z$ are the spin-1 and spin-$\frac{1}{2}$ Pauli matrices, respectively, and $A_\parallel$ is the coupling strength[32]. Applying the rotating wave approximation, we transform into the reference frame rotating at $\frac{1}{2}\omega_{\mathrm{mech}} = \frac{1}{2}(2\gamma b + \Delta)$ where $\Delta$ gives the detuning of $\omega_{\mathrm{mech}}$ from the $|+1\rangle \leftrightarrow |-1\rangle$ spin state splitting. Diagonalizing the resulting Hamiltonian gives eigenstates $\{0, m, p\}$ with energies $\{-D, -\frac{1}{2}\sqrt{(\Omega+\delta\Omega)^2 + \xi_\pm^2}, \frac{1}{2}\sqrt{(\Omega+\delta\Omega)^2 + \xi_\pm^2}\}$ where $\xi_\pm \equiv \Delta + 2\gamma\delta b \pm A_\parallel$ for the $m_I = \pm\frac{1}{2}$ sublevel of the $^{13}$C manifold. Here, $\gamma/2\pi = 2.8$ MHz/G is the NV center gyromagnetic ratio and $D \simeq D_0 + \frac{dD}{dT}\Delta T$ is the zero-field splitting where $D_0/2\pi = 2.87$ GHz and $\frac{dD}{dT} = -74\times 2\pi$ kHz/°C is the temperature dependence of $D$[20,33–35]. Appendix B provides a more detailed derivation of the mechanically dressed Hamiltonian.

Fig. 1c plots the energy levels of the dressed and undressed eigenstates as a function of both $\gamma\delta b$ and $\Delta/2$. The Larmor frequency $\omega_{i,j}$ at which a qubit accumulates phase is given by the energy splitting between the $|i\rangle$ and $|j\rangle$ qubit states. Variations in $\delta b$ will cause $\omega_{i,j}$ to fluctuate in time, dephasing the qubit. Mechanically dressing the NV center opens an avoided crossing between the $|m\rangle$ and $|p\rangle$ states at $\gamma\delta b = \frac{1}{2}(\Delta \pm A_\parallel)$, which reduces the sensitivity of $\omega_{i,j}$ to variations in $\delta b$ and protects the qubit from dephasing.

## III. DEVICE DETAILS

We use a high-overtone bulk acoustic resonator (HBAR) to generate the large amplitude ac lattice strain needed to coherently drive NV center spin transitions. Our mechanical resonator is fabricated from a type IIa, ⟨100⟩-oriented diamond specified to contain fewer than 5 ppb nitrogen impurities. A uniform distribution of individually addressable NV centers was introduced via irradiation with 2 MeV electrons at a fluence of $\sim 1.2 \times 10^{14}$ cm$^{-2}$ followed by annealing at 850°C for 2 hours. The NV centers studied in this work are located at a depth of $\sim 47$ $\mu$m.

In contrast to our previous studies of spectroscopic[23] and coherent[27] interactions between an NV center ensemble and a mechanical resonator, here we study the coherence of a single NV center under a continuous mechanical drive. By measuring a single NV center, we eliminate the inhomogeneity in $\Omega$ that arises when the depth-dependent amplitude of the stress standing wave addresses a spatially distributed NV center ensemble. Although NV center ensembles provide advantages in fluorescence level and could be protected using mechanical CDD, we choose to study single NV centers because they provide the cleanest possible system in which to study the underlying physics of mechanical CDD.

The HBAR used in these measurements consists of a 3 $\mu$m thick ⟨002⟩-oriented ZnO film sandwiched between a Ti/Pt (25 nm/200 nm) ground plane and an Al (250 nm) top contact. The piezo-electric ZnO film transduces stress waves into the diamond. The diamond then acts as an acoustic Fabry-Pérot cavity to create stress standing wave resonances. Fig. 2a shows a network analyzer measurement of the HBAR admittance ($Y_{11}$) plotted as a function of frequency. From this frequency comb, we selected the $\omega_{\mathrm{mech}}/2\pi = 586$ MHz resonance mode, which has the combination of quality factor ($Q = 2700$ as calculated by the $Q$-circle method[36]) and on-resonance impedance (18 Ω) expected to produce the largest mechanical driving fields. This resonance suppresses driving field amplitude noise that is faster than $\omega_c = \frac{\omega_{\mathrm{mech}}}{2Q} = 110 \times 2\pi$ kHz.

A microwave antenna patterned from Ti/Pt (25 nm/225 nm) on the diamond face opposite the

ZnO transducer provides gigahertz frequency magnetic fields for conventional magnetic spin control. Fig. 2b shows a schematic depiction of the final device, and additional device details are provided in Appendix C.

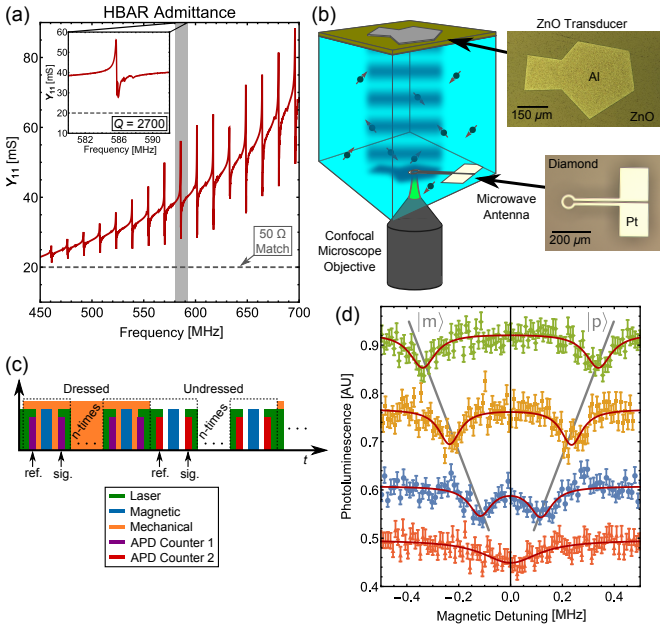


FIG. 2. (a) Network analyzer measurement of the power admitted to the HBAR. The inset highlights the $\omega_{\rm mech}/2\pi = 586$ MHz mode used in the measurements. (b) Device schematic. (c) Pulse sequence used for dressed state spectroscopy measurements. (d) Spectra of the $|0\rangle \leftrightarrow |m\rangle$ and $|0\rangle \leftrightarrow |p\rangle$ spin transitions within the dressed state basis. From bottom to top, the mechanical driving fields are $\Omega/2\pi = 0$ kHz, $\Omega/2\pi = 230 \pm 10$ kHz, $\Omega/2\pi = 470 \pm 8$ kHz, and $\Omega/2\pi = 670 \pm 10$ kHz.

## IV. DRESSED STATE SPECTROSCOPY

We spectroscopically observe the emergence of the dressed states by first tuning the $m_I = +1$ $^{14}N$ sublevel of the $|+1\rangle \leftrightarrow |-1\rangle$ splitting into resonance with the $\omega_{\rm mech}/2\pi = 586$ MHz mechanical mode[23]. We then perform dressed state spectroscopy using the concatenated pulse sequence in Fig. 2c. In a single instance of this sequence, the NV center is optically initialized into the $|0\rangle$ spin state at which point a reference fluorescence measurement is made of the full-scale NV center photoluminescence. A magnetic $\pi$-pulse of strength $\Omega_{\rm mag}/2\pi \sim 80$ kHz is then applied to drive a conditional spin rotation. Finally, fluorescence readout provides a quantitative measure of the spin population remaining in $|0\rangle$. We interleave $n$ instances of this pulse sequence executed in the dressed basis with $n$ instances of this pulse sequence executed in the undressed basis. In a typical experiment $n \sim 10$, giving a total duty cycle time of $\sim 280$ $\mu$s and mechanical pulse length of $\sim 140$ $\mu$s. This pulse duration is much longer than the 1.5 $\mu$s ring time of our resonator, ensuring a fully rung up resonator. We differentiate between the dressed and undressed signal by routing the photon counts from our avalanche photodiode (APD) to separate data acquisition counters. This sequence is then repeated as a function of the magnetic detuning $\Delta_{\rm mag}$ from the $|0\rangle \leftrightarrow |-1\rangle$ state splitting. The resulting spectra are shown in Fig. 2d for several values of $\Omega$. The data have been fit using the procedure described in Appendix D.

By simultaneously measuring $\omega_{0,-1}$; $\omega_{0,m}$; and $\omega_{0,p}$, we can feedback on $b$ to precisely zero $\Delta$ using the relation $\frac{1}{2}(\omega_{0,m} + \omega_{0,p}) - \omega_{0,-1} = \frac{1}{2}\Delta$ (see Appendix E for a derivation). Operating at $\Delta = 0$ where $\frac{\partial \omega_{i,j}}{\partial \delta b}\Big|_{\Delta=0} \neq 0$ detunes $\Omega$ equally from each $^{13}$C sublevel. This dresses both sublevels equivalently, preserving the full spin contrast of our measurements and maintaining the $^{13}$C manifold as a degree of freedom. Alternatively, we could maximally protect one nuclear sublevel at the expense of the other by operating at $\Delta = \pm A_\parallel$ where $\frac{\partial \omega_{i,j}}{\partial \delta b}\Big|_{\Delta=\pm A_\parallel} = 0$ for one of the two sublevels. For an unpolarized $^{13}$C spin, however, such a strategy would halve the measured spin contrast, limiting the utility of mechanical CDD.

## V. COHERENCE OF THE $\{0, p\}$ QUBIT

Next, we perform Ramsey measurements within the dressed basis to quantify the decoherence protection offered by mechanical CDD. We begin by examining the qubit derived from the $\{0, p\}$ subspace, which is minimally perturbed from the more familiar $\{0, -1\}$ qubit.

The pulse sequence used for these measurements is shown in Fig. 3a. After optically initializing the spin into $|0\rangle$, we apply a magnetic $\pi/2$-pulse of strength $\Omega_{\rm mag}/2\pi = 700$ kHz to populate the $\{0, p\}$ subspace. Because $\Omega_{\rm mag} > \omega_{m,p}$, the $\{0, m\}$ subspace is also populated. After a free evolution time $\tau$, we apply a second magnetic $\pi/2$-pulse of the same strength to return the spin population to $|0\rangle$ where the signal is read out optically. To help visualize the decay, we advance the phase of the second $\pi/2$-pulse by $\omega_{\rm rot}\tau$. Undressed Ramsey measurements are interleaved with the dressed measurements to reduce the average power load and provide a simultaneous measurement of the undressed dephasing time $T^*_{2,\{0,-1\}}$. We then repeat this sequence as a function of $\tau$ to generate a single CDD Ramsey curve.

Fig. 3b shows that a $\Omega/2\pi = 348 \pm 4$ kHz dressing field extends $T_2^*$ from $5.9 \pm 0.4$ $\mu$s to $15.0 \pm 0.9$ $\mu$s. As described in Appendix D, we approximate the decay of our CDD Ramsey signal with a Gaussian envelope. This is not strictly correct because $\omega_{0,p}$ varies non-linearly with $\delta b$. Nevertheless, when $\frac{\partial \omega_{i,j}}{\partial \delta b} \neq 0$ Gaussian decay reasonably approximates the dephasing over the range of $\Omega$ employed in this work and facilitates comparison with the undressed qubit coherence. Fig. 3c,d provide the Fourier

spectrum of each measurement in Fig. 3b. Beating in the undressed Ramsey signal reveals a $|A_\parallel|/2\pi = 145 \pm 6$ kHz coupling to a nearby $^{13}$C spin.

If the $\{0,p\}$ qubit coherence is limited by $\delta b$, then $T^*_{2,\{0,p\}}$ should scale linearly with $\Omega$. However, as Fig. 3e shows, plotting $T^*_{2,\{0,p\}}$ as a function of $\Omega$ reveals an erratic distribution with a clustering around $T^*_{2,\{0,p\}} \sim 12$ $\mu$s. By monitoring the temperature of our sample over the course of several measurements as described in Appendix F, we identified that this effect arises from $\sim 0.25$°C long-term temperature instabilities. Temperature enters the dressed NV center Hamiltonian through the zero-field splitting $D$, which varies at a rate of $\frac{dD}{dT} = -74 \times 2\pi$ kHz/°C[20,34,35] and contributes to $\omega_{0,p}$ and $\omega_{0,m}$. Gaussian thermal drift with a standard deviation of $\sigma_T = 0.25$°C will dephase the $\{0,p\}$ qubit in $T^*_{2,\{0,p\}} = \frac{\sqrt{2}}{\sigma_T dD/dT} = 12$ $\mu$s. Coherence times measured during periods of minimal thermal drift exceed this limit, indicating that mechanical CDD isolates the $\{0,p\}$ qubit from magnetic noise more successfully than Fig. 3e implies. Thermal instabilities take over as the dominant dephasing channel, however, which suggests mechanical CDD could offer an alternative thermometry protocol to thermal CPMG[20].

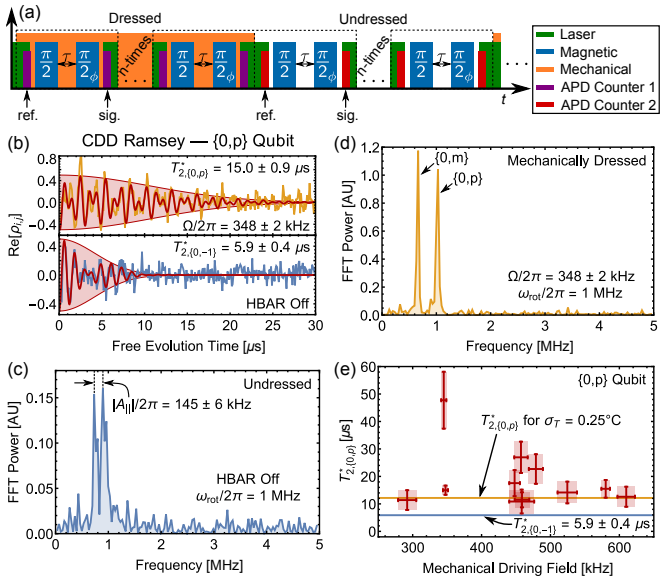


FIG. 3. (a) Pulse sequence used for CDD Ramsey measurements of the $\{0,p\}$ qubit. (b) Ramsey measurements of the $\{0,p\}$ qubit protected by a $\Omega/2\pi = 348 \pm 2$ kHz mechanical dressing field and the $\{0,-1\}$ qubit. (c,d) Fourier spectra of the Ramsey data in (b). (e) Coherence time of the $\{0,p\}$ qubit plotted as a function of $\Omega$. Error bars in (e) indicate 95% confidence intervals.

## VI. COHERENCE OF THE $\{m,p\}$ QUBIT

With the $\{0,p\}$ qubit subdued by thermal fluctuations, we turn to the $\{m,p\}$ qubit to fully explore the efficacy of mechanical CDD at enhancing $T_2^*$. The Larmor frequency $\omega_{m,p}$ is independent of $D$, making the $\{m,p\}$ qubit insensitive to changes in temperature and thus capable of exceeding the $\sim 12$ $\mu$s thermally-limited coherence.

Fig. 4a shows the pulse sequence used to measure $T^*_{2,\{m,p\}}$. Here, magnetic double quantum (DQ) $\pi$-pulses of frequency $\omega_{DQ} = \frac{1}{2}(\omega_{0,m} + \omega_{0,p})$ and strength $\Omega_{\rm mag}/2\pi = 1.51$ MHz address the $\{m,p\}$ subspace[37]. We interleave the dressed $\{m,p\}$ Ramsey measurements with undressed measurements that execute the same sequence of magnetic pulses. Because this pulse sequence amounts to a $2\pi$ rotation of the undressed $\{0,-1\}$ qubit, the average of this undressed trace $\langle P_{0,U}\rangle$ quantifies the NV center spin contrast.

During each measurement of $T^*_{2,\{m,p\}}$, we periodically measure $\Delta$ spectroscopically and feedback on $b$ to maintain $\Delta \sim 0$. Interpolating linear drift between these measurements, we post-select to include only those data sets for which $\sigma_\Delta/2\pi < 60$ kHz and $|\langle\Delta\rangle|/2\pi < 35$ kHz. For these measurements, we studied a second NV center located nearby the NV center that was used in the $\{0,p\}$ qubit measurements. Both NV centers are quantitatively similar and have comparable $T^*_{2,\{0,-1\}}$ and $A_\parallel$.

Fig. 4b shows a typical CDD Ramsey measurement for the $\{m,p\}$ qubit that has been fit using the procedure described in Appendix D. The undressed analog of the $\{m,p\}$ qubit is the $\{+1,-1\}$ qubit, and its $T^*_{2,\{+1,-1\}} = 2.7 \pm 0.1$ $\mu$s coherence time (measurement details in Appendix G) is indicated by the shaded region in Fig. 4b. A $\Omega/2\pi = 581 \pm 2$ kHz dressing field extends the $\{m,p\}$ qubit coherence to $T^*_{2,\{m,p\}} = 15 \pm 1$ $\mu$s.

## VII. DECOHERENCE MODEL

In order to quantitatively study how the measured spin protection scales with $\Omega$, we examine quasi-static deviations in $\omega_{i,j}$[38]. Because we work in a reference frame rotating at $\frac{1}{2}\omega_{\rm mech}$, low frequency electric and strain field noise are averaged away, and—as noted above—the $\{m,p\}$ qubit is isolated from thermal noise. We thus examine dephasing from only two independent sources: $\delta b$ and $\delta\Omega$.

Generically, first order deviations in the Larmor frequency $\omega_{i,j}$ take the form $\delta\omega_{i,j} = \alpha\delta x$ where $\alpha$ is a constant. If the fluctuation $\delta x$ follows a Gaussian distribution with standard deviation $\sigma_x$, an expression for the associated dephasing rate can be found by calculating the weighted average of a distribution of detuned,

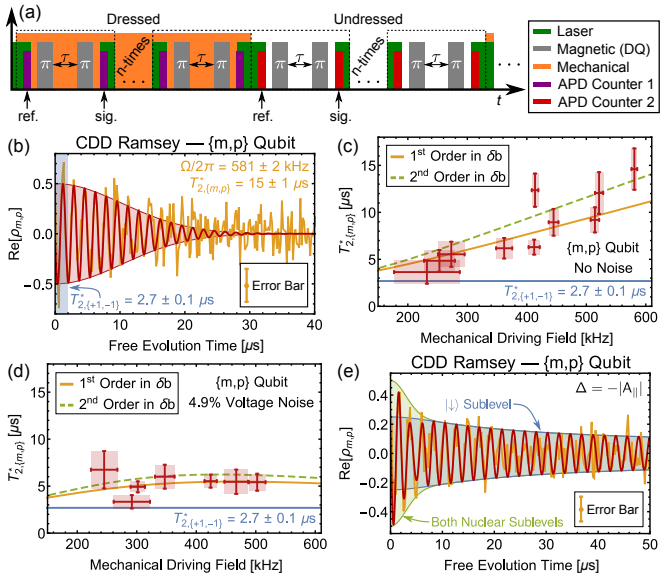


FIG. 4. (a) Pulse sequence used for CDD Ramsey measurements of the $\{m,p\}$ qubit. (b) Ramsey measurements of the $\{m,p\}$ qubit protected by a $\Omega/2\pi = 581 \pm 2$ kHz mechanical dressing field. (c,d) Coherence time of the $\{m,p\}$ qubit plotted as a function of $\Omega$ for measurements where $\Omega$ was (c) actively stabilized and (d) given a Gaussian noise profile. Error bars in (c,d) indicate 95% confidence intervals. (e) Ramsey measurement of the $\{|m,\downarrow\rangle, |p,\downarrow\rangle\}$ qubit protected by a $\Omega/2\pi = 455.7 \pm 0.5$ kHz mechanical dressing field under the condition $\Delta = -|A_\parallel|$.

un-damped Ramsey signals:

$$\begin{aligned}\mathrm{Re}[\rho_{i,j}] &= \frac{1}{\sqrt{2\pi}\sigma_x}\int e^{-\frac{\delta x^2}{2\sigma_x^2}}\cos\left[(\omega_{i,j}+\alpha\delta x)\tau\right]\mathrm{d}\delta x \\ &= e^{-\frac{1}{2}(\alpha\sigma_x\tau)^2}\cos\left(\omega_{i,j}\tau\right).\end{aligned} \tag{1}$$

Comparing Eq. 1 with an ideal Ramsey signal given by $\mathrm{Re}[\rho_{i,j}] = e^{-\frac{\tau^2}{T_2^{*2}}}\cos(\omega_{i,j}\tau)$, we see that $T_2^* = \frac{\sqrt{2}}{\alpha\sigma_x}$ and therefore $\Gamma_x = \frac{2\pi}{T_2^*} = \sqrt{2}\pi\alpha\sigma_x$. The dephasing time from a collection of uncorrelated noise sources is given by $\frac{1}{T_2^*} = \frac{1}{2\pi}\sum\Gamma_i$.

For the high electronic purity CVD diamond studied in this work, the NV center undressed $T_2^*$ is limited by dipolar coupling to nearby $^{13}$C nuclear spins[39]. This coupling can be approximately modeled by a random time-varying magnetic field that follows a Gaussian distribution[30]. For magnetic field fluctuations experienced by the $\{0,-1\}$ qubit, we can then set $\alpha\delta x \to \gamma\delta b$ and arrive at the size of the $^{13}$C spin bath $\gamma\sigma_b/2\pi = (\sqrt{2}\pi T_{2,\{0,-1\}}^*)^{-1} = 42 \pm 2$ kHz where $T_{2,\{0,-1\}}^* = 5.4 \pm 0.3$ $\mu$s for this NV center.

In the dressed basis, expanding $\omega_{m,p}$ to first order in $\delta b$ gives

$$\delta\omega_{m,p;b} = \frac{2|A_\parallel|\gamma\delta b}{\sqrt{A_\parallel^2+\Omega^2}}, \tag{2}$$

from which we find $\Gamma_b = 2\sqrt{2}\kappa|A_\parallel|/T_{2,\{0,-1\}}^*$ where $\frac{1}{\kappa} = \frac{1}{\sqrt{2}\pi}\sqrt{A_\parallel^2+\Omega^2}$. Similarly, expanding $\omega_{m,p}$ to first order in $\delta\Omega$ gives

$$\delta\omega_{m,p;\Omega} = \frac{\Omega\delta\Omega}{\sqrt{A_\parallel^2+\Omega^2}}, \tag{3}$$

from which we find $\Gamma_\Omega = \kappa\Omega\sigma_\Omega$.

Our measurements of $T_{2,\{m,p\}}^*$ employ a feedback protocol to level the power supplied to the HBAR and reduce $\delta\Omega$ to $\sim 0.03\%$ of $\Omega$. For the range of $\Omega$ accessed here, this level of stability makes $\Gamma_\Omega \ll \Gamma_b$, and we can ignore the effects of $\delta\Omega$. To first order in $\delta b$, the dephasing time of the $\{m,p\}$ qubit is then given by $T_{2,\{m,p\}}^* = \frac{2\pi}{\Gamma_b}$.

Fig. 4c plots $T_{2,\{m,p\}}^*$ as a function of $\Omega$. The measurements used to obtain each data point are presented in Appendix H, and we attribute scatter in the data mainly to deviations from the $\Delta = 0$ condition. For $\Omega \lesssim 10\gamma\sigma_b = (420 \pm 20) \times 2\pi$ kHz, the first order expansion in $\delta b$ correctly predicts $T_{2,\{m,p\}}^*$. However, as $\Omega$ increases and $\frac{\partial\omega_{m,p}}{\partial\delta b}\Big|_{\Delta=0}$ diminishes, the measured coherence times begin to surpass the predictions of the first order model. To account for this, we extend our model to second order in $\delta b$ as detailed in Appendix I and numerically solve the resulting non-Gaussian decoherence envelope for the $\frac{1}{e}$ decay time[38]. As seen in Fig. 4c, the model correct to second order in $\delta b$ more accurately predicts $T_{2,\{m,p\}}^*$ for $\Omega \gtrsim 10\gamma\sigma_b$. This suggests that for these higher dressing fields, the $\{m,p\}$ qubit coherence remains limited by $\delta b$. The cw power handling capabilities of our device prohibited measurements at larger $\Omega$, but these results indicate that $T_{2,\{m,p\}}^*$ would continue to increase with $\Omega$.

To test the predictive capabilities of our model, we intentionally increase $\delta\Omega$ to the point where $\Gamma_\Omega$ becomes the dominant dephasing channel. To do this quantitatively, we monitor the voltage reflected from the HBAR $V_R$, which scales linearly with $\Omega$. We then periodically randomize the power supplied to the HBAR to give $V_R$ a Gaussian distribution with standard deviation $\sigma_V = \eta\langle V_R\rangle$ where $\eta$ is a constant. This yields a Gaussian distribution of $\Omega$ with a standard deviation $\sigma_\Omega = (\langle\Omega\rangle + \alpha)\eta$ where $\alpha/2\pi = -133 \pm 7$ kHz is a constant related to our measurement of $V_R$ as described in Appendix J. The dephasing time is then given by $T_{2,\{m,p\}}^* = \frac{2\pi}{\Gamma_b+\Gamma_\Omega}$.

Fig. 4d shows the measured and predicted $T_{2,\{m,p\}}^*$ for $\eta = 4.9 \pm 0.2\%$. Once again, the measurements used to obtain each data point are presented in Appendix H. Decoherence in these measurements is dominated by $\delta\Omega$. Therefore, the model accurately predicts

$T^*_{2,\{m,p\}}$ whether $\Gamma_b$ is correct to first or second order in $\delta b$. Power leveling can effectively zero $\delta\Omega$ over the range of $\Omega$ measured here, but these results suggest that in a more efficient device where a larger $\Omega$ is attainable, amplitude noise would eventually limit the protection that mechanical CDD offers, even in the power-leveled case.

## VIII. PROTECTING A SINGLE $^{13}$C SUBLEVEL

We conclude by maximally protecting the $|\downarrow\rangle$ $^{13}$C sublevel of the $\{m,p\}$ qubit at the expense of the $|\uparrow\rangle$ sublevel. By setting $\Delta = -|A_\parallel|$ where $|A_\parallel|/2\pi = 150 \pm 4$ kHz for this NV center, we establish the condition $\frac{\partial\omega_{m,p}}{\partial\delta b}\Big|_{\Delta=-|A_\parallel|} = 0$ for the $|\downarrow\rangle$ sublevel. As described in Appendix I, to second order in $\delta b$ the coherence of this sublevel is then described by[38]

$$\mathrm{Re}[\rho_{m,p;\downarrow}] = \frac{\langle P_{0,U}\rangle}{4}\sqrt{\frac{\Omega}{\sqrt{\Omega^2+(2\gamma\sigma_b)^4\tau^2}}}\cos\left[\Omega\tau+\phi\right]. \tag{4}$$

The result of this measurement for a $\Omega/2\pi = 455.7 \pm 0.5$ kHz dressing field is shown in Fig. 4e. As detailed in Appendix I, the data have been fit to a sum of Eq. 4, Gaussian decay of the $|\uparrow\rangle$ coherence, and a constant background $c$. Only the parameters $\Omega$, $\phi$, $c$, and $T^*_{2,\uparrow}$ were allowed to vary as free parameters in our fitting procedure.

As the shaded regions of Fig. 4e highlight, the $|\uparrow\rangle$ sublevel rapidly dephases in $T^*_{2,\uparrow} = 4.1 \pm 0.7$ $\mu$s, while the coherence of the $|\downarrow\rangle$ sublevel is strongly protected, persisting beyond the 50 $\mu$s time frame of the measurement. This marks a $\gtrsim$ 19-fold increase in $T^*_{2,\{m,p\}}$ over the bare $T^*_{2,\{+1,-1\}}$. We note that infidelities in our DQ pulses reduce the spin contrast within this subspace, limiting the utility of protecting only one sublevel in an unpolarized hyperfine manifold. Higher fidelity pulsing protocols or more efficient photon collection[40] could increase the signal-to-noise ratio, which would make the lengthy coherence of the $\{|m,\downarrow\rangle, |p,\downarrow\rangle\}$ qubit a valuable asset.

## IX. CONCLUSIONS

In summary, we have experimentally demonstrated and theoretically analyzed the performance of mechanical CDD for decoupling an NV center spin qubit. We have shown that ac lattice strain can dress the spin states of an NV center and that the eigenstates of this dressed basis have robust coherence even in the presence of magnetic field fluctuations. We prolong $T_2^*$ of a thermally isolated qubit from $2.7 \pm 0.1$ $\mu$s to $15 \pm 1$ $\mu$s with a $\Omega/2\pi = 581 \pm 2$ kHz mechanical dressing field and show that $T_2^*$ can be extended even further by either engineering more efficient devices or choosing to protect only a single $^{13}$C hyperfine sublevel. Mechanical CDD preserves the $|0\rangle$ state and therefore does not require the NV center to be adiabatically dressed and undressed before and after each measurement. Moreover, the thermally sensitive $\{0,p\}$ and $\{0,m\}$ qubits maintain the gigahertz-scale Larmor frequency of their undressed analogs, providing rapid signal accumulation for a dressed state thermometer. Mechanically dressed qubits thus offer a promising option in the continuing development of NV center technology.

## ACKNOWLEDGMENTS

We thank J. Maxson, A. Bartnik, B. Dunham, and I. Bazarov at the Cornell University Cornell Laboratory for Accelerator-Based Sciences and Education (CLASSE) for electron irradiating the diamond sample used in this work for the creation of NV centers. We thank P. Maletinksy for interesting and useful discussions. Research support was provided by the Office of Naval Research (ONR) (Grant N000141410812). ERM received support from the Department of Energy Office of Science Graduate Fellowship Program (DOE SCGF), made possible in part by the American Recovery and Reinvestment Act of 2009, administered by ORISE-ORAU under contract no. DE-AC05-06OR23100. Device fabrication was performed in part at the Cornell NanoScale Science and Technology Facility, a member of the National Nanotechnology Coordinated Infrastructure, which is supported by the National Science Foundation (Grant ECCS-15420819), and at the Cornell Center for Materials Research Shared Facilities which are supported through the NSF MRSEC program (DMR-1120296).

### Appendix A: Mechanical Rabi Driving

The mechanically driven Rabi oscillations depicted in Fig. 1a were measured using the pulse sequence shown in Fig. 5. As described in detail in Ref.[27], the relatively high $Q$ of our mechanical resonance makes it difficult to perform a traditional pulsed Rabi measurement. Instead, a pair of magnetic $\pi$-pulses resonant with the $|0\rangle \leftrightarrow |-1\rangle$ transition and separated by a fixed time $\tau_{\mathrm{mag}}$ is swept through a fixed-length mechanical pulse. The mechanical pulse drives the $|+1\rangle \leftrightarrow |-1\rangle$ spin transition, and the duration of this interaction is set by the area of the mechanical pulse enclosed between the two $\pi$-pulses. By knowing the shape of the mechanical pulse and tracking the delay $\tau_0$ of the magnetic pulse pair, we convert this enclosed area to effective square-pulse units or an "effective mechanical pulse length." Because the mechanical resonator is pulsed in this experiment, we are able to achieve a larger driving field than in the continuous dynamical decoupling (CDD) Ramsey measurements where the mechanical resonator operates in cw mode.

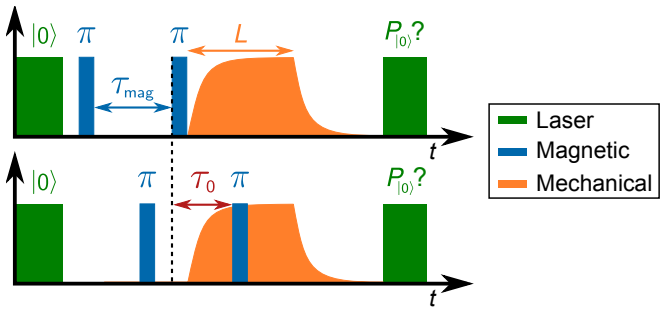


FIG. 5. Pulse sequence used to measure mechanically driven Rabi oscillations.

## Appendix B: Mechanically Dressed Hamiltonian

As mentioned in Section II, we work within the $m_I = +1$ sublevel of the $^{14}$N hyperfine manifold. We consider both a static magnetic field $b$ that is aligned along the NV center symmetry axis and subject to fluctuations $\delta b$ and a mechanical driving field $\Omega$ that is subject to amplitude fluctuations $\delta\Omega$. In the $\{+1, 0, -1\} \otimes \{(m_I =) + \frac{1}{2}, -\frac{1}{2}\}$ Zeeman basis, a nearby $^{13}$C nuclear spin weakly couples to an NV center electronic spin through the hyperfine perturbation $H_C = A_\parallel S_z I_z$ where $S_z$ and $I_z$ are the spin-1 and spin-$\frac{1}{2}$ Pauli matrices, respectively, and $A_\parallel$ is the coupling strength[32]. An NV center electronic spin then obeys the Hamiltonian

$$H_{LF} = \begin{pmatrix} \gamma b_\Sigma + \frac{1}{2}A_\parallel & 0 & 0 & 0 & \Omega_\Sigma \cos(\omega_{\rm mech} t) & 0 \\ 0 & \gamma b_\Sigma - \frac{1}{2}A_\parallel & 0 & 0 & 0 & \Omega_\Sigma \cos(\omega_{\rm mech} t) \\ 0 & 0 & -D & 0 & 0 & 0 \\ 0 & 0 & 0 & -D & 0 & 0 \\ \Omega_\Sigma \cos(\omega_{\rm mech} t) & 0 & 0 & 0 & -\gamma b_\Sigma - \frac{1}{2}A_\parallel & 0 \\ 0 & \Omega_\Sigma \cos(\omega_{\rm mech} t) & 0 & 0 & 0 & -\gamma b_\Sigma + \frac{1}{2}A_\parallel \end{pmatrix}$$

where $b_\Sigma = b + \delta b$, $\Omega_\Sigma = \Omega + \delta\Omega$, other parameters are as previously defined, and we have not included a magnetic driving field. Applying the rotating wave approximation and transforming into the reference frame rotating at $\frac{1}{2}\omega_{\rm mech} = \frac{1}{2}(2\gamma b + \Delta)$ gives the Hamiltonian in the rotating frame

$$H_{RF} = \begin{pmatrix} \gamma b_\Sigma + \frac{1}{2}(\Delta + A_\parallel) & 0 & 0 & 0 & \frac{1}{2}\Omega_\Sigma & 0 \\ 0 & \gamma b_\Sigma + \frac{1}{2}(\Delta + A_\parallel) & 0 & 0 & 0 & \frac{1}{2}\Omega_\Sigma \\ 0 & 0 & -D & 0 & 0 & 0 \\ 0 & 0 & 0 & -D & 0 & 0 \\ \frac{1}{2}\Omega_\Sigma & 0 & 0 & 0 & -\gamma b_\Sigma - \frac{1}{2}(\Delta + A_\parallel) & 0 \\ 0 & \frac{1}{2}\Omega_\Sigma & 0 & 0 & 0 & -\gamma b_\Sigma - \frac{1}{2}(\Delta - A_\parallel) \end{pmatrix}.$$

Diagonalizing $H_{RF}$ gives the mechanically dressed Hamiltonian whose energies are quoted in Section II:

$$H_D = \begin{pmatrix} -D & 0 & 0 & 0 & 0 & 0 \\ 0 & -D & 0 & 0 & 0 & 0 \\ 0 & 0 & -\frac{1}{2}\sqrt{\Omega_\Sigma^2 + \xi_-^2} & 0 & 0 & 0 \\ 0 & 0 & 0 & \frac{1}{2}\sqrt{\Omega_\Sigma^2 + \xi_-^2} & 0 & 0 \\ 0 & 0 & 0 & 0 & -\frac{1}{2}\sqrt{\Omega_\Sigma^2 + \xi_+^2} & 0 \\ 0 & 0 & 0 & 0 & 0 & \frac{1}{2}\sqrt{\Omega_\Sigma^2 + \xi_+^2} \end{pmatrix}$$

where $\xi_\pm = \Delta + 2\gamma\delta b \pm A_\parallel$. In the limit $\Omega_\Sigma = 0$, $H_D$ reduces to the undressed Zeeman Hamiltonian in the rotating frame.

## Appendix C: Additional Device Details

Our device was fabricated with an in-house procedure designed to create high $Q$ resonances with good impedance matches to a 50 Ω line. For a fixed input

power to the device, a resonance with a higher $Q$ and a better impedance match will produce a larger amplitude stress standing wave and thus a larger mechanical driving field. This scaling can be approximated by the expression[23]

$$\frac{\Omega_1}{\Omega_2} = \frac{Q_1}{Q_2} \times \frac{Z_1\sqrt{50\ \Omega + Z_2}}{Z_2\sqrt{50\ \Omega + Z_1}} \tag{C1}$$

where $\Omega_i$ is the mechanical driving field, $Z_i$ is the impedance, and $Q_i$ is the quality factor of the $i^{\text{th}}$ resonance. Using this expression, we selected the $\omega_{\text{mech}}/2\pi = 586$ MHz resonance mode, which was expected to give the largest mechanical driving fields.

## Appendix D: Fitting Functions

### 1. Dressed State Spectroscopy

The dressed state spectra displayed in Fig. 2d are fit to the sum of two Lorentzians

$$P_D = c_D - \frac{a_{D,p}}{\left(\omega - \frac{1}{2}\sqrt{\Delta^2+\Omega^2} - \frac{1}{2}\Delta - \omega_{0,-1}\right)^2 + \left(\frac{1}{2}\Gamma_D\right)^2} - \frac{a_{D,m}}{\left(\omega + \frac{1}{2}\sqrt{\Delta^2+\Omega^2} - \frac{1}{2}\Delta - \omega_{0,-1}\right)^2 + \left(\frac{1}{2}\Gamma_D\right)^2} \tag{D1}$$

where $P_D$ is the measured photoluminescence, $c_D$ is a constant background, $\omega_{0,-1}$ is the undressed $|0\rangle \leftrightarrow |-1\rangle$ spin state splitting, $\Delta$ is the mechanical detuning, $\Omega$ is the mechanical driving field, $a_{D,i}$ accounts for the depth of the $i^{\text{th}}$ spectral peak, and $\Gamma_D$ measures the full width at half maximum of the dressed spectral peaks. The undressed signal accumulated from the interleaved measurements is simultaneously fit to the Lorentzian

$$P_U = c_U - \frac{a_U}{(\omega - \omega_{0,-1})^2 + \left(\frac{1}{2}\Gamma_U\right)^2}. \tag{D2}$$

We then subtract $\omega_{0,-1}$ from the $x$-axis to plot photoluminescence as a function of $\Delta_{\text{mag}}$.

### 2. Undressed Ramsey Measurements

We fit the undressed Ramsey data in Fig. 3b and Fig. 6a to the expression

$$P_{\{0,-1\}} = c - \frac{a}{4}e^{-\frac{\tau^2}{T_2^{*2}}}\left\{\cos\left[\left(\omega_{\text{rot}} + \Delta_{\text{mag}} + \frac{1}{2}A_\parallel\right)\tau\right] + \cos\left[\left(\omega_{\text{rot}} + \Delta_{\text{mag}} - \frac{1}{2}A_\parallel\right)\tau\right]\right\} \tag{D3}$$

where $P_{\{0,-1\}}$ is the measured photoluminescence, $c$ is a constant background, $a$ is an overall amplitude that accounts for deviations from perfect spin contrast, $\Delta_{\text{mag}}$ is the magnetic detuning, and $A_\parallel$ quantifies coupling to an unpolarized $^{13}$C nuclear spin. Of these values, $c$, $a$, $T_2^*$, $\Delta_{\text{mag}}$, and $A_\parallel$ are free parameters in our fit. We use the values of $a$ and $c$ returned from the fits to rescale the $y$-axes in terms of the qubit coherence $\text{Re}[\rho_{0,-1}]$.

### 3. CDD Ramsey Measurements: $\{0,p\}$ Qubit

To fit the CDD Ramsey data for the $\{0,p\}$ qubit, we zero the magnetic detuning midway between the $^{13}$C sublevels. Assuming $\Delta = 0$, our $\{0,p\}$ CDD Ramsey signal is then described by the expression

$$P_{\{0,p\}} = c + \frac{1}{4}e^{-\frac{\tau^2}{T_2^{*2}}}\left\{a_p\cos\left[\left(\Delta_{\text{mag}} + \omega_{\text{rot}}\right)\tau + \phi\right] + a_m\cos\left[\left(\Delta_{\text{mag}} + \omega_{\text{rot}} + \sqrt{\Omega^2 + A_\parallel^2}\right)\tau + \phi\right]\right\} \tag{D4}$$

where $a_p$ is the spin contrast for the $\{0,p\}$ qubit, $a_m$ is the spin contrast for the $\{0,m\}$ qubit, $\phi$ is a constant phase offset, and the other parameters are as defined above. The undressed Ramsey data fixes the value of $A_\parallel$, and we vary $c$, $a_i$, $\phi$, $\Omega$, and $\Delta_{\text{mag}}$ as free parameters in our fitting procedure. We use the values of $a_m$, $a_p$, and $c$ returned from the fit to rescale the $y$-axis of Fig. 3b in terms of $\text{Re}[\rho_{0,p}]$.

### 4. CDD Ramsey Measurements: $\{m,p\}$ Qubit

Fixing $\Delta = 0$, we fit the $\{m,p\}$ qubit data shown in Fig. 4b, Fig. 7, and Fig. 8 to the expression

$$P_{\{m,p\}} = c + \frac{\langle P_{0,U}\rangle}{2}e^{-\frac{\tau^2}{T_2^{*2}}}\cos\left[\tau\sqrt{A_\parallel^2 + \Omega^2} + \phi\right] \tag{D5}$$

where the parameters are as defined above. We allow $c$, $T_2^*$, $\Omega$, and $\phi$ to vary as free parameters in our fitting procedure, and we use $\langle P_{0,U}\rangle$ and the value of $c$ returned from the fits to rescale the $y$-axes of our plots in terms of $\text{Re}[\rho_{m,p}]$.

## Appendix E: Expression for the Mechanical Detuning

In our spectroscopy measurements, we use the relation $\frac{1}{2}(\omega_{0,m} + \omega_{0,p}) - \omega_{0,-1} = \frac{1}{2}\Delta$ as a means of zeroing the mechanical detuning. To derive this expression, we begin in the $\{+1, 0, -1\}$ basis with the Hamiltonian for an NV center subject to both a mechanical driving field and a magnetic driving field resonant with the $|0\rangle \leftrightarrow |-1\rangle$ transition. In the doubly rotating reference frame, this can

be written

$$H_{RF} = \begin{pmatrix} \frac{1}{2}\Delta & 0 & \frac{1}{2}\Omega \\ 0 & -D-\Delta_{\rm mag} & \frac{1}{2}\Omega_{\rm mag} \\ \frac{1}{2}\Omega & \frac{1}{2}\Omega_{\rm mag} & -\frac{1}{2}\Delta \end{pmatrix} \qquad \text{(E1)}$$

where $\Delta_{\rm mag} = -\frac{1}{2}\Delta$ for resonant magnetic driving, and $\Omega_{\rm mag}$ is far enough detuned from the $|+1\rangle \leftrightarrow |0\rangle$ transition that we can ignore the $\langle +1| H_{RF} |0\rangle$ matrix element.

For the undressed case ($\Omega = 0$, $\Delta = 0$), the energy of the $|0\rangle \leftrightarrow |-1\rangle$ splitting in this reference frame is $\omega_{0,-1} = D$ where we define $\hbar = 1$. With $\Omega \neq 0$, calculating the eigenvalues of Eq. E1 to first order in $\frac{\Omega_{\rm mag}}{\Omega}$ gives energies $\omega_{0,p} = D + \frac{1}{2}(\Delta + \sqrt{\Delta^2+\Omega^2})$ and $\omega_{0,m} = D + \frac{1}{2}(\Delta - \sqrt{\Delta^2+\Omega^2})$. From this we arrive at the desired expression $\frac{1}{2}(\omega_{0,m} + \omega_{0,p}) - \omega_{0,-1} = \frac{1}{2}\Delta$. The same expression is obtained when the $^{13}$C coupling is included.

### Appendix F: Thermal Stability

As mentioned in Section VI, we intersperse spectral measurements within CDD Ramsey measurements of the $\{m,p\}$ qubit. This allows us to feedback on $b$ and maintain a relatively constant $\Delta$, but these measurements also quantify the thermal drift over the course of the measurement. A histogram of $\Delta$ extracted from fitting these spectra to Eq. D1 quantifies drift in the magnetic bias field as $\sigma_\Delta = 2\gamma\sigma_{\rm bias}$ where $\sigma_\Delta$ and $\sigma_{\rm bias}$ are the standard deviations of the $\Delta$ histogram and of the magnetic bias field, respectively. A histogram of $\omega_{0,-1}$, however, provides information about both the magnetic bias field drift and the thermal drift according to

$$\sigma_{0,-1} = \sqrt{(\gamma\sigma_{\rm bias})^2 + \left(\frac{dD}{dT}\sigma_T\right)^2} \qquad \text{(F1)}$$

where $\sigma_T$ is the standard deviation of normally distributed thermal drift, $\frac{dD}{dT} = -74 \times 2\pi$ kHz/°C is the temperature dependence of $D$[20,34,35], and $\sigma_{0,-1}$ is the standard deviation of the $\omega_{0,-1}$ histogram. The average of $\sigma_T$ for the power-leveled data that satisfy our post-selection criteria is $0.25 \pm 0.03$°C. Thermal drift on a similar scale can be expected for the $\{0,p\}$ qubit measurements.

Applying the findings of Section VII to thermal dephasing of the $\{0,p\}$ qubit, we find that for Gaussian thermal fluctuations, $\alpha\delta x \rightarrow \frac{dD}{dT}\delta T$. Fluctuations on the scale of $\sigma_T$ would thus limit the $\{0,p\}$ qubit coherence time to $T^*_{2,\{0,p\}} = \frac{\sqrt{2}}{\sigma_T dD/dT} = 12 \pm 1$ $\mu$s as quoted in Section V.

### Appendix G: Coherence of the $\{+1,-1\}$ Qubit

We compare the coherence of the $\{m,p\}$ qubit to that of the undressed $\{+1,-1\}$ qubit because in each of these qubits both component states are sensitive to magnetic field fluctuations. Directly measuring the dephasing time of the $\{+1,-1\}$ qubit at nonzero field with high precision is a non-trivial task because the measurement becomes sensitive to double quantum pulse infidelities. Instead, we measure $T_2^*$ of the undressed $\{0,-1\}$ qubit (Fig. 6) and rely on the fact that for Gaussian magnetic field fluctuations $T^*_{2,\{+1,-1\}} = \frac{1}{2}T^*_{2,\{0,-1\}}$. This gives $T^*_{2,\{+1,-1\}} = 2.7 \pm 0.1$ $\mu$s as quoted in Section VI. This same undressed Ramsey measurement also quantifies $|A_\parallel|/2\pi = 150 \pm 4$ kHz and $\sigma_b = 2.4 \pm 0.1$ mG for this NV center.

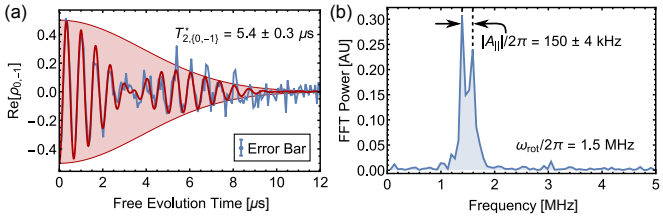


FIG. 6. (a) Ramsey measurement of the undressed $\{0,-1\}$ qubit for the NV center used in the $\{m,p\}$ qubit measurements. (b) Fourier spectrum of (a).

### Appendix H: $\{m,p\}$ Qubit CDD Ramsey Data

The data and fits from the measurements of $T^*_{2,\{m,p\}}$ shown in Fig. 4c,d are displayed in Fig. 7 and Fig. 8, respectively.

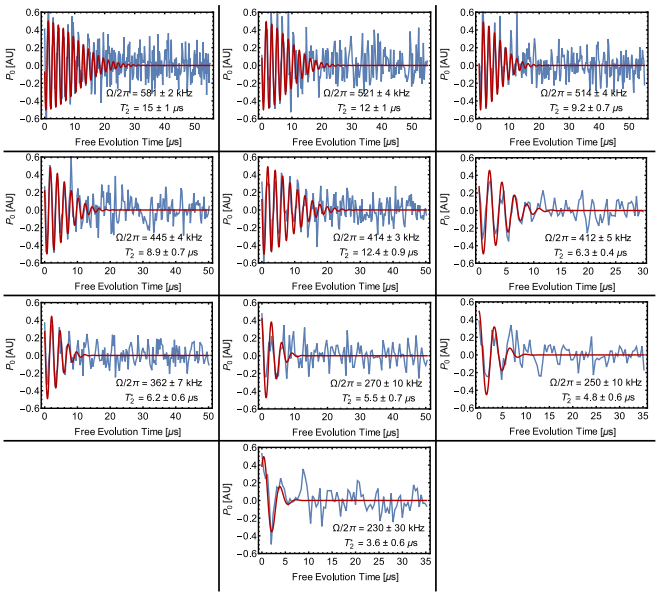


FIG. 7. Data and fits for CDD Ramsey measurements of the $\{m,p\}$ qubit when $\Omega$ was actively stabilized.

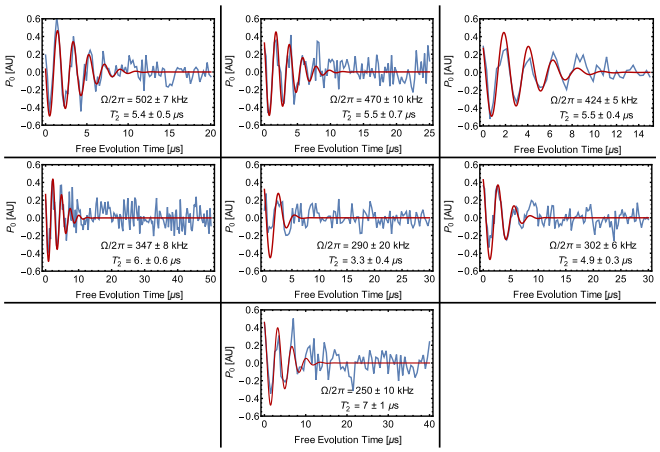


FIG. 8. Data and fits for CDD Ramsey measurements of the $\{m,p\}$ qubit when $\Omega$ was given a Gaussian noise profile.

## Appendix I: Second Order Magnetic Field Fluctuations

The decay envelope of a Ramsey measurement is given by the expression $f(\tau,\Omega,\sigma_b,A_\parallel) = |\langle e^{i\delta\phi}\rangle|$ where $\delta\phi$ is the random phase accumulated in a given duty cycle of the measurement[38]. For the $\{m,p\}$ qubit in the case when $\Delta = 0$ and $\delta\Omega = 0$, the Larmor frequency is $\omega_{m,p} = \sqrt{\Omega^2 + (A_\parallel + 2\gamma b)^2}$. To second order in $\delta b$, fluctuations in $\omega_{m,p}$ from magnetic field fluctuations are then given by

$$\begin{aligned}\delta\omega_{m,p} &= \frac{\partial\omega_{m,p}}{\partial b}\Big|_{\delta b=0}\delta b + \frac{\partial^2\omega_{m,p}}{\partial b^2}\Big|_{\delta b=0}\frac{\delta b^2}{2} + O(\delta b^3) \\ &= \frac{2\gamma\delta b(A_\parallel^3 + A_\parallel\Omega^2 + \gamma\delta b\Omega^2)}{(A_\parallel^2+\Omega^2)^{3/2}}\end{aligned}, \tag{I1}$$

and the random phase accumulated is $\delta\phi = \delta\omega_{m,p}\tau$. By averaging this phase over a Gaussian distribution of magnetic field fluctuations, we find an expression for the decoherence envelope

$$\begin{aligned}f(\tau,\Omega,\sigma_b,A_\parallel) &= \left|\frac{1}{\sqrt{2\pi}\sigma_b}\int_{-\infty}^{\infty} e^{i\delta\omega_{m,p}\tau}e^{-\frac{\delta b^2}{2\sigma_b^2}}\,\mathrm{d}\delta b\right| \\ &= \sqrt{\beta}e^{-\frac{2(\gamma\sigma_b A_\parallel\beta\tau)^2}{A_\parallel^2+\Omega^2}}\end{aligned} \tag{I2}$$

where

$$\beta(\tau,\Omega,\sigma_b,A_\parallel) \equiv \sqrt{\frac{(A_\parallel^2+\Omega^2)^3}{(A_\parallel^2+\Omega^2)^3 + (2\gamma\sigma_b\Omega)^4\tau^2}}. \tag{I3}$$

To produce the second order model curves in Fig. 3b,c, we numerically solve this expression for the value of $\tau$ such that $f(\tau,\Omega,\sigma_b,A_\parallel) = \frac{1}{e}$.

When $\Delta = -|A_\parallel|$, the two $^{13}$C sublevels follow different decay envelopes that can be computed by setting $A_\parallel \to 0$ and $A_\parallel \to 2A_\parallel$ in Eq. I2. In the former case, $f(\tau,\Omega,\sigma_b,0)$ reduces to

$$h(\tau,\Omega,\sigma_b) = \sqrt{\frac{\Omega}{\sqrt{\Omega^2+(2\gamma\sigma_b)^4\tau^2}}} \tag{I4}$$

as seen in Section VIII. For the case of $A_\parallel \to 2A_\parallel$, we approximate the decay as Gaussian. The fitting function for Fig. 4e then becomes

$$\begin{aligned}P_{\{m,p\}} = \frac{\langle P_{0,U}\rangle}{4}\Bigg\{&\sqrt{\frac{\Omega}{\sqrt{\Omega^2+(2\gamma\sigma_b)^4\tau^2}}}\cos\left[\Omega\tau+\phi\right] \\ &+ e^{-\frac{t^2}{T_{2,\uparrow}^{*2}}}\cos\left[\tau\sqrt{\Omega^2+4A_\parallel^2}+\phi\right]\Bigg\} + c\end{aligned} \tag{I5}$$

where only $\Omega$, $\phi$, $c$, and $T_{2,\uparrow}^*$ were allowed to vary as free parameters. We use $\langle P_{0,U}\rangle$ and the value of $c$ returned from the fit to rescale the $y$-axis of Fig. 4e in terms of $\mathrm{Re}[\rho_{m,p}]$.

For simplicity, this derivation of $f(\tau,\Omega,\sigma_b,A_\parallel)$ does not include driving field noise. Including amplitude noise in the mechanical driving field on the scale of our power-leveled measurements produces no noticeable change in the results of the model over the range of mechanical driving fields addressed here.

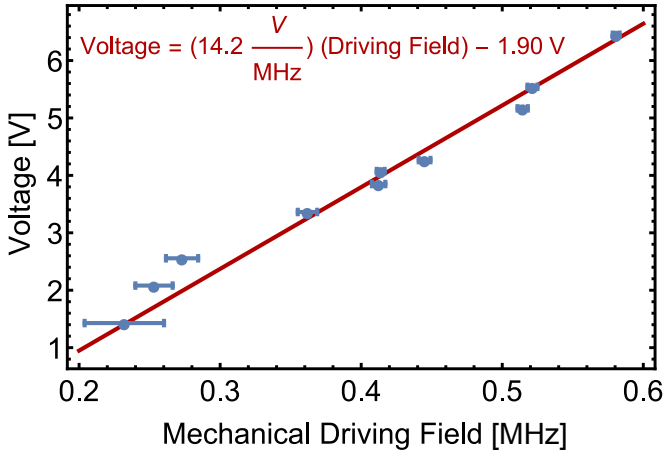


FIG. 9. Voltage reflected from the mechanical resonator plotted as a function of the mechanical driving field.

## Appendix J: Measuring the Voltage Reflected from the HBAR

We monitor the mechanical driving field amplitude by tracking the RF power reflected from the mechanical resonator. An RF circulator redirects the reflected power to

an RF diode that converts the ac signal into the dc voltage that we measure. As shown in Fig. 9, this measured voltage scales linearly with the mechanical driving field. However, due to the diode's nonzero threshold voltage, that linear dependence has a nonzero intercept.

We introduce driving field noise to our experiment by periodically shifting the applied power such that the spread of voltages measured by the RF diode over the course of a measurement is normally distributed with a standard deviation of $\eta\langle V_R\rangle$ where $V_R$ is the reflected voltage and $\eta$ is a constant. Because Fig. 9 has a nonzero intercept, such a distribution of voltages will correspond to a Gaussian distribution of driving fields with a standard deviation of $\sigma_\Omega = (\langle\Omega\rangle + \alpha)\eta$ where $\alpha/2\pi = -133 \pm 7$ kHz is the ratio of the intercept to the slope for the line of best fit in Fig. 9.

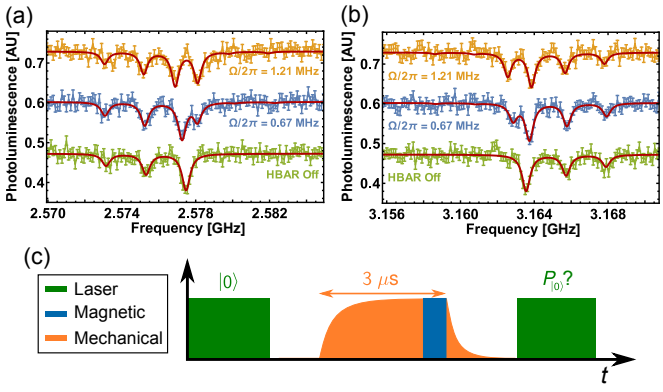


FIG. 10. (a) Dressed state spectrum for a magnetic pulse swept through the undressed $|0\rangle \leftrightarrow |-1\rangle$ transition. (b) Dressed state spectrum for a magnetic pulse swept through the undressed $|+1\rangle \leftrightarrow |0\rangle$ transition. (c) Pulse sequence used in these measurements.

## Appendix K: Dressed Spectra Through the $|+1\rangle \leftrightarrow |0\rangle$ Transition

Fig. 10 shows spectral measurements of the dressed state splitting as measured by sweeping the detuning of a $\Omega_{\rm mag}/2\pi = 350$ kHz magnetic pulse through the resonance of the undressed (a) $|0\rangle \leftrightarrow |-1\rangle$ and (b) $|+1\rangle \leftrightarrow |0\rangle$ transitions. All three $^{14}$N hyperfine sublevels are visible in the spectra. Because $\omega_{\rm mech}$ is tuned into resonance with the $|(m_s =) + 1, (m_I =) + 1\rangle \leftrightarrow |-1, +1\rangle$ transition within the $^{14}$N hyperfine manifold, only the $m_I = +1$ peak splits into the dressed states $|m, +1\rangle$ and $|p, +1\rangle$. In these measurements, the HBAR was powered in 3 $\mu$s pulses as shown in Fig. 10c. This reduced the average power load and allowed us to reach higher driving fields than we were able to reach in the CDD Ramsey experiments where the mechanical resonator operates in a pseudo-cw mode.

* gdf9@cornell.edu


[1] V. V. Dobrovitski, G. D. Fuchs, A. L. Falk, C. Santori, and D. D. Awschalom, Annu. Rev. Cond. Mat. Phys. **4**, 23-50 (2013).

[2] R. Schirhagl, K. Chang, M. Loretz, and C. L. Degen, Annu. Rev. Phys. Chem. **65**, 83-105 (2014).

[3] L. Childress, M. V. G. Dutt, J. M. Taylor, A. S. Zibrov, F. Jelezko, J. Wrachtrup, P. R. Hemmer, and M. D. Lukin, Science **314**, 5797 (2006).

[4] G. de Lange, Z. H. Wang, D. Ristè, V. V. Dobrovitski, and R. Hanson, Science **330**, 6000 (2010).

[5] C. A. Ryan, J. S. Hodges, and D. G. Cory, Phys. Rev. Lett. **105**, 200402 (2010).

[6] G. de Lange, D. Ristè, V. V. Dobrovitski, and R. Hanson, Phys. Rev. Lett. **106**, 080802 (2011).

[7] B. Naydenov, F. Dolde, L. T. Hall, C. Shin, H. Fedder, L. C. L. Hollenberg, F. Jelezko, and J. Wrachtrup, Phys. Rev. B **83**, 081201(R) (2011).

[8] Z.-H. Wang, G. de Lange, D. Ristè, R. Hanson, and V. V. Dobrovitski, Phys. Rev. B **85**, 155204 (2012).

[9] T. van der Sar, Z. H. Wang, M. S. Blok, H. Bernien, T. H. Taminiau, D. M. Toyli, D. A. Lidar, D. D. Awschalom, R. Hanson, and V. V. Dobrovitski, Nature **484**, 82 (2012).

[10] P. Rabl, P. Cappellaro, M. V. G. Dutt, L. Jiang, J. R. Maze, and M. D. Lukin, Phys. Rev. B **79**, 041302(R) (2009).

[11] F. Dolde, H. Fedder, M. W. Doherty, T. Nöbauer, F. Rempp, G. Balasubramanian, T. Wolf, F. Reinhard, L. C. L. Hollenberg, F. Jelezko, and J. Wrachtrup, Nat. Phys. **7**, 459 (2011).

[12] N. Timoney, I. Baumgert, M. Johanning, A. F. Varón, M. B. Plenio, A. Retzker, and C. Wunderlich, Nature **476**, 185 (2011).

[13] H. Fedder, F. Dolde, F. Rempp, T. Wolf, P. Hemmer, F. Jelezko, and J. Wrachtrup, Appl. Phys. B **102**, 497 (2011).

[14] X. Xu, Z. Wang, C. Duan, P. Huang, P. Wang, Y. Wang, N. Xu, X. Kong, F. Shi, X. Rong, and J. Du, Phys. Rev. Lett. **109**, 070502 (2012).

[15] M. Hirose, C. D. Aiello, and P. Cappellaro, Phys. Rev. A **86**, 062320 (2012).

[16] V. V. Mkhitaryan and V. V. Dobrovitski, Phys. Rev. B **89**, 224402 (2014).

[17] D. A. Golter, T. K. Baldwin, and H. Wang, Phys. Rev. Lett. **113**, 237601 (2014).

[18] Y. Matsuzaki, X. Zhu, K. Kakuyanagi, H. Toida, T. Shimo-Oka, N. Mizuochi, K. Nemoto, K. Semba, W. J. Munro, H. Yamaguchi, and S. Saito, Phys. Rev. Lett. **114**, 120501 (2015).

[19] V. V. Mkhitaryan, F. Jelezko, and V. V. Dobrovitski, arXiv:1503.06811v1 (2015).

[20] D. M. Toyli, C. F. de las Casas, D. J. Christle, V. V. Dobrovitski, and D. D. Awschalom, Proc. Natl. Acad. Sci. USA **110**, 8417 (2013).

[21] P. Ovartchaiyapong, L. M. A. Pascal, B. A. Myers, P. Lauria, and A. C. B. Jayich, Appl. Phys. Lett. **101**, 163505 (2012).

[22] M. J. Burek, D. Ramos, R. Patel, I. W. Frank, and M. Lǒncar, Appl. Phys. Lett. **103**, 131904 (2013).

[23] E. R. MacQuarrie, T. A. Gosavi, N. R. Jungwirth, S. A. Bhave, and G. D. Fuchs, Phys. Rev. Lett. **111**, 227602 (2013).

[24] J. Teissier, A. Barfuss, P. Appel, E. Neu, and P. Maletinsky, Phys. Rev. Lett. **113**, 020503 (2014).

[25] P. Ovartchaiyapong, K. W. Lee, B. A. Myers, and A. C. B. Jayich, Nat. Commun. **5**, 4429 (2014).

[26] S. Meesala, Y.-I. Sohn, H. A. Atikian, S. Kim, M. J. Burek, J. T. Choy, and M. Lǒncar, arXiv:1511.01548 (2015).

[27] E. R. MacQuarrie, T. A. Gosavi, A. M. Moehle, N. R. Jungwirth, S. A. Bhave, and G. D. Fuchs, Optica **2**, 233-238 (2015).

[28] A. Barfuss, J. Teissier, E. Neu, A. Nunnenkamp, and P. Maletinsky, Nat. Phys. **11**, 820 (2015).

[29] J.-M. Cai, B. Naydenov, R. Pfeiffer, L. P. McGuinness, K. D. Jahnke, F. Jelezko, M. B. Plenio, and A. Retzker, New J. Phys. **14**, 113023 (2012).

[30] C. D. Aiello, M. Hirose, and P. Cappellaro, Nat. Commun. **4**, 1419 (2013).

[31] S. K. Mishra, L. Chotorlishvili, A. R. P. Rau, and J. Berakdar, Phys. Rev. A **90**, 033817 (2014).

[32] C. P. Slichter, *Principles of Magnetic Resonance*, 3rd ed. (Springer, 1996).

[33] M. W. Doherty, F. Dolde, H. Fedder, F. Jelezko, J. Wrachtrup, N. B. Manson, and L. C. L. Hollenberg, Phys. Rev. B **85**, 205203 (2012).

[34] V. M. Acosta, E. Bauch, M. P. Ledbetter, A. Waxman, L.-S. Bouchard, and D. Budker, Phys. Rev. Lett. **104**, 070801 (2010).

[35] M. W. Doherty, V. M. Acosta, A. Jarmola, M. S. J. Barson, N. B. Manson, D. Budker, and L. C. L. Hollenberg, Phys. Rev. B **90**, 041201 (2014).

[36] D. A. Feld, R. Parker, R. Ruby, P. Bradley, and S. Dong, in *Ultrasonics, IEEE Symposium* (2008).

[37] H. J. Mamin, M. H. Sherwood, M. Kim, C. T. Rettner, K. Ohno, D. D. Awschalom, and D. Rugar, Phys. Rev. Lett. **113**, 030803 (2014).

[38] G. Ithier, E. Collin, P. Joyez, P. J. Meeson, D. Vion, D. Esteve, F. Chiarello, A. Shnirman, Y. Makhlin, J. Schriefl, and G. Schön, Phys. Rev. B **72**, 134519 (2005).

[39] A. Bermudez, F. Jelezko, M. B. Plenio, and A. Retzker, Phys. Rev. Lett. **107**, 150503 (2011).

[40] P. Siyushev, F. Kaiser, V. Jacques, I. Gerhardt, S. Bischof, H. Fedder, J. Dodson, M. Markham, D. Twitchen, F. Jelezko, and J. Wrachtrup, Appl. Phys. Lett. **97**, 241902 (2010).